Hierarchical color similarity metrics for step-wise application on sky monitoring surface cameras

S. L. Mantelli Neto [1,2], A. C. Sobieranski [2], E. B. Pereira [1], A. von Wangenheim [2]

[1]INPE Brazilian National Institute for Space Research
Av. dos Astronautas 1758 São José dos Campos SP Brazil 12227-010
[2]UFSC Federal University of Santa Catarina
Campus Universitário Trindade, Florianópolis SC Brazil 88040-900

Key Points:

- Most methods existent on literature for surface camera cloud assessments uses dichotomic results and discards one dimension of colour space
- Those methods are adopted because domain monitored is logarithmic and cameras linear devices causing distortions and saturation to fit range
- We proposed a new method based on atmospheric scattering dealing with pixel distortions and full color space use reducing analysing errors

Corresponding author: Sylvio Luiz Mantelli Neto, `sylvio@lepten.ufsc.br`

Abstract

Digital cameras on the surface are frequently used for monitoring atmospheric conditions. Several methods were developed to use the images for synoptic observations, cloud assessments, short term forecasting and so on. However, there are some restrictions not considered by these methods, especially when a linear camera is used to observe logarithmic ranges of atmospheric luminance. Cameras accommodate the scene to a linear scale causing distortions on pattern distributions by pixel value saturation (PVS) and drifts from its original hues. This brings on some simplifying practices commonly found in the literature to overcome these problems. But those practices result in loss of data, misinterpretation of valid pixels and restriction on the use of computer vision algorithms. The present work begins by illustrating these problems performing supervised learning for two reasons: all observation systems seek out automation of human synoptic observation in order to provide a sound mathematical modeling of the observed patterns. A new modeling paradigm is proposed to map the sky patterns to represent the existent physical atmospheric phenomena not considered by the literature. We validate the proposed method, and compared the results using 1630 images against two well-established methods. A hypothesis test showed that results are compatible with currently used binary approach with advantages. Differences were due to PVS and other restrictions not considered by the methods existent on literature. Finally, the present work concludes that the new paradigm presents more meaningful results of sky patterns interpretation, allows extended daylight observation periods and uses a higher dimensional space.

1 Introduction

The observation of current atmospheric conditions from the surface is an important feature to be monitored, especially in order to assess cloud coverage, amount and category. These parameters are especially important in the climate research area (Kasten & Czeplak, 1980), (Marty & Philipona, 2000), (Bojanowski et al., 2013), atmospheric physical models (Harrison et al., 2008), (Nardino & Georgiadis, 2003), (Yamanouchi & Charlock, 1993), (Cess et al., 1995) and validation of satellite-based resources (Martins et al., 2007), (Martins et al., 2003). Clouds are also a major source of uncertainty in the assessment of solar energy (Hu & Stamnes, 2000). In particular, a considerable effort has been spent on computer-based methods able to assess *nowcasting* conditions.

Synoptic observation (SO) is one activity always present on monitoring stations. SO evaluation of clouds is usually performed by humans and is highly subjective and variable (WMO, 2008, chap. 15). For these reasons, several research groups have been aiming at replacing a highly human-dependent activity through cameras and computer-based methods. The World Meteorological Organization (WMO) calls continuous sky monitoring equipment Synoptic Observation Systems (SOS) (WMO, 2008). SOSs usually employ all-sky digital cameras, algorithms, and methods for continuous monitoring (Bradley et al., 2010). Several commercial types of equipment are being used for this purpose at considerable costs, such as: Total Sky Imager-(TSI) (http://www.yesinc.com/products/data/tsi880/index.html), Whole Sky Imager-(WSI) (http://www.arm.gov/instruments/wsi, MOONGLOW (http://www.allskycam.com/index.php) and so on. Some research groups are trying to find more affordable equipment and better surface image-based methods for cloud detection.

Surface based sky pattern analysis, however, has been restricted when automated systems are used to reproduce the human qualitative analysis of the environment. It is important to evaluate what could actually be classified with present methods due to system limitations.

When focusing on cloud detection and quantification, the most common outcome expected from automated image analysis approaches found in the literature is the clas-

sification of image into cloud or sky patterns. This kind of pixel value-based classifier that classifies pixel values in either one or other category by thresholding is a *dichotomizer* as shown by (Duda et al., 2001, sec.2.4.2). Authors noticed by observation the presence of more than two patterns present on color space representing other physical *phenomena* (i.e. red, yellow, etc) that are not cloud and sky patterns (white and blue) (S. Mantelli, 2001; Naylor, 2002). These additional *phenomena* are misclassified by dichotomous non-hierarchical methods. This moved the authors to find a more adequate approach to deal with systemic technological restrictions.

The present work focuses on cloud detection and quantification. If no proper cloud detection method is used, there is no meaning going on more complex cloud classification. The objective will be on the evaluation of computer-based methods using cameras to quantify the clouds like: computer vision, digital image processing and machine learning (ML) algorithms. An extended analysis using additional sensors and methods for cloud assessments could be observed on the review made by Tapakis and Charalambides (2013).

In our approach the sky observation will be replaced by a computational model centered on a new hierarchical color similarity measure that matches SOS's functions. We propose tackling the problem of developing a more reliable SOS through a broader and more systemic analysis, considering not only the computer algorithms to quantify the clouds, but also the monitoring sensor, its capabilities to observe the environment, and its possible outcomes.

2 Objectives

The objectives of this work are

- to evaluate present surface camera-based methods for the quantification of clouds that employ computer vision and related approaches for digital image processing, and cloud coverage analysis and
- to propose a new hierarchical partially non-isotropic color space model that overcomes some of the shortcomings of those models.

In this context, our paper offers two main contributions:

- we demonstrate the existence of patterns representing physical phenomena registered by surface cameras by performing an exploratory data analysis (EDA) on customized color spaces based upon pattern occurrences;
- we propose a novel hierarchical image analysis method to characterize these patterns that takes into consideration atmospheric, optics and surface camera limitations.

The validation of our approach was performed through comparison to methods described in the literature, which we implemented and compared to our results. This comparison was possible through reducing the color space dimension of the results obtained by our approach when comparing our results to the results achieved through traditional methods for nearly 1630 images.

In the next paragraphs we will describe the role of luminance in the system, the experimental set-up and propose a new set of patterns that could be perceived from images acquired through state-of-the-practice equipment. We will base our model on the atmospheric optical physics theory (Naylor, 2002), abandoning a simple dichotomized approach.

3 State of the Art

A commonly used cloud pattern classification method is value thresholding (VT). It is based on pixel values or their combination in order to determine whether a given pixel represents a cloud or clear sky area. VT was used by (Souza-Echer et al., 2006) with classification criterion based on the saturation (S) dimensions only out of Hue, Saturation and Lightness (HSL) color space. Hue and Lightness pixel dimensions were discarded, restricting the cloud and sky patterns variability on the task at hand (Newell & Simon, 1971) to only one dimension (1-D. A variation of VT was developed by (Kazantzidis et al., 2012) using the difference $R-B$ between red (R) and blue (B) pixel dimensions on Red, Green and Blue (RGB) color space to classify pixels into cloud or sky patterns. Only the green dimension was discarded and the variability of the cloud/sky patterns were restricted to two dimensions (2D). If pixel dimensions are reduced to the (R,B) plane, their correspondent color range is also reduced to a range varying from black to magenta, instead of black to white (Gonzalez & Woods, 2007, sec 6.2.1) in the color space. A classification method based on *linear thresholding* (LT) was developed in (H. W. S. J. Johnson R., 1989.). It used normalized Red (R) and Green (G) pixel dimensions R/B to classify pixels into cloud or sky patterns. The limitations of these methods are the same already described by $2D$ usage of color space. But VT and LT are simpler, easily reproducible and widely used for data comparison between methods.

More elaborated methods based on machine learning have also been proposed to discriminate between cloud and clear sky patterns. An approach employing *neural networks* (NNs) trained upon training sets obtained from previously classified images containing RGB values normalized by clear sky models, as described by (Iqbal, 1983), was developed in order to classify sky images (S. Mantelli, 2001; S. L. Mantelli et al., 2005). The work presented in (Cazorla et al., 2008) also used NNs with optimized parameters by means of *genetic algorithms* (GA) to identify the same two classes, *sky* and *cloud*. The parameters were obtained from a variance matrix $9x9$ of R and average values of R and B dimensions only. But NN and GA methods depend heavily on a large set of implementation conditions, not easily replicated, unless these parameters (training sets, NN configuration, etc.) are supplied in detail by the original authors. NN is a powerful computational resource when correctly modeled, and is can be executed in parallel due to the nature of the technique. On the other side, the use of NN as a linear or nonlinear mapper, could be methodologically misleading due to its black-box working simply like a linear regression method. Some authors reported difficulties on the adequate parametric representation of the problem caused by the complex structure of NNs (Johannet et al., 2007; Qiu & Jensen, 2004; Setiono et al., 2000), while others indicate semantic errors during the development of specific applications (Jain et al., 2000; Zhang, 2007). Improper or restricted modeling of task environment and inadequate size of training sets, together with lack of sound mathematical base can lead NN to useless results. One problem with dichotomizing is the two class problem solution. Any pixel value existent in the observation domain that does not belong to one or either class, is randomly misplaced in some of them. (Cazorla et al., 2015) also developed an adaptive method to classify sky images. (Yang et al., 2016) used background subtraction together with an adaptive thresholding to evaluate current conditions to detect clouds. Parameters for the adaptive thresholding were obtained from a set of clear sky reference images. Another problem is that, according to (Reinhard et al., 2005; Mitsunaga & Nayar, 1999) sky luminance range spans nearly 5 orders of magnitude, from 10^1 to 10^5 cd/m^2. If we consider that typical cameras are capable of monitoring luminance values of approximately 2 orders of magnitude, from 0 to 10^2, it becomes clear that, in order for an adaptive method using cameras to span the entire scale of logarithmic luminance in discrete steps (multi-exposure approach), approximately $s = \frac{10^5}{10^2} = 10^3$ steps will be necessary.

The luminance variation in the sky is intense, non-uniform, and dependent on angular and atmospheric conditions (Perez et al., 1993). All the methods mentioned above

present difficulties and even errors (Sabburg & Wong, 1999), leading to a deteriorating SOS performance in classifying patterns, especially near the higher intensity regions. The authors additionally understand that the reduction of dimensionality produced by $1D$ and $2D$ color-spaces also aggravates these problems, restricting analysis range and pruning data variability, preventing a more detailed analysis. Some authors prefer to avoid this kind of situation removing higher intensity regions from image analysis by *"manual cropping"* (Qingyong et al., 2011, sec. 2.a). Other authors used the same *"manually cropped"* method and extended it to all-sky images (Marquez & Coimbra, 2013), ignoring that such approach does not configure an *all-weather* method. In that case, the analysis, performed by a dichotomizer, is optimized to work only on a subset of the environment captured by all-sky systems. Ceiling all-sky images by cropping higher intensity regions removes a significant amount of information from the image analysis process. This phenomenon will later be illustrated on figure 1 and these pixels will be defined as pertaining to two disctinct color-subspaces: *Diffusion of Non-Specific Scattering* (**DNSS**) and *Diffusion of Rayleigh Scattering* (**DRAY**) patterns (Grossberg & Nayar, 2003). Another aspect described in (Qingyong et al., 2011) is that, when a part of the images used for the analysis are taken manually by different operators under distinct camera exposition adjusts, an adaptive method seems to be appropriate to compensate the variable image acquisition exposition adjusted manually.

Some digital image processing methods like background subtraction (Piccardi, 2004) and spatial geometric *locus* (S. L. Mantelli et al., 2010) were also used to detect clouds. Background subtraction is a computer vision technique commonly used on image detection of moving objects using a static background. An automated cloud detection method based on the green channel or $1D$ of total-sky visible images (Yang et al., 2015, 2016) mentioned a better performance of thin clouds detection. Although the article recognized effects of Rayleigh and Mie scattering on image acquisition, no formal treatment is mentioned on regions with saturated pixel values. Spatial geometric locus of patterns on color space deals with the full dimensional range of color space and do not use dichotomizing. The classification results also show patterns in luminance gradients, but they are also restricted by a mapping into three separate classes.

Other methods assisted by physical models like (Mejia et al., 2016) and (Kurtz et al., 2017) employs supervised learning and analysis. Learning process is implemented from a Radiative Transfer Model (RTM) and simulated images of various cloud optical depth (τ_c). Authors also considered different solar ($\mathcal{V}_s$) and pixel ($\mathcal{V}_z$) position related to camera zenith angle (θ_0). But although the method pointed out some new and important features to be used on image analysis and not used in our work, it still uses only a $2D$ color space based upon *Radiance Red Blue Ratio* (RRBR), losing information. Another important consideration used by the method is the adjust of saturated pixels to 1, meaning that every saturated pixel is supposed to be a cloud (Mejia et al., 2016, sec. 5.1). According to our observations, pixels representing clear sky pixels also saturate and drift from their original hues at the end of the color scale, also presenting PVS.

Additional methods, employing multispectral approaches combining infrared cameras, polarimeters and Longwave (LW) have also been used to support surface cameras (Feister et al., 2000; Feister & Shields, 2005; Schade et al., 2008; Kreuter et al., 2009). Nevertheless, the image classification methods used employ the same approach of pixelwise value-based segmentation using linear thresholding mentioned previously. These methods focus on different discriminating functions but keep the same dichotomizing approach.

However, our experience has demonstrated that false positives, false negatives, non-classifiable patterns and more than two simultaneous patterns are always present in the task environment, and are not adequately handled by a dichotomizer. Dichotomizers also do not allow the definition of uncertainty and errors by parametric analysis nor handle multi-category patterns. Another limitation of these approaches is the reduction of di-

mensionality, underestimating the resources existent on the task environment causing loss of information, performance reduction, and increased error (Jain et al., 2000).

3.1 The role of sky luminance of images taken from the surface

The independent variables analyzed by automated systems using cameras are the image pixel values in the *RGB* color space (Gonzalez & Woods, 2002). In a color image each pixel represents a 3-dimensional data unit of 24 bits/pixel with 8 bits or 255 digital number values (DN) for every color dimension, representing a total of 256^3 different colors. However, only 256 and 256^2 colors are available from respectively 1-dimensional and 2-dimensional counterpart classification methods. We understand that a higher-dimensional pixel representation, preserving acquired data, can better describe the variability of these data and improve the quality of pattern classification in the color space. The luminance axis of DN values, for example, scale relatively to the main diagonal of color space. Luminance is limited to a range of $\sqrt{256^2 + 256^2 + 256^2} = 443.40$ for the RGB cube in color images with 8 bits per channel (S. L. Mantelli Neto, 2010). For a 2-dimensional model employing typical 8 bit per channel color codification, on the other side, only a projection of the RB diagonal $\sqrt{256^2 + 256^2} = 362.03$ is available. An increase of pixel resolution using a finer camera will improve the image quality, but will not affect the luminance scale of the system due to the limited span of the color domain. This restriction is valid for any image resolution. Algorithms that could be used to determine cloud height and type would also have its performance downgraded by dimensional reduction.

Cameras and displays are not able to sense and reproduce the luminance scale existent on natural scenes (Tsin et al., 2001; Koslof, 2006; Inanici & Navvab, 2006), reducing the overall amount of useful data. That restriction causes pixel value saturation (PVS) [1], pattern distribution distortions and difficulties when applying digital image processing algorithms, ML methods (i.e. neural networks, fuzzy logic, genetic algorithms and so on) or statistical analysis. These restrictions also apply to file structures registering the information representing the images; i.e. JPG, PNG, BMP. Table 1 illustrates some light conditions existent in natural scenes that could be perceived by the human eye.

Table 1. Levels of luminance found in some external environment. Source: (Reinhard et al., 2005, chap. 1 tab. 1.1).

Condition	**luminance** cd/m^2
Starlight	10^{-3}
Moonlight	10^{-1}
Internal Illumination	10^{2}
Sunlight	10^{5}
Maximum intensity of CRT monitors	10^{2}

The table shows that natural scenes span luminances up to eight orders of magnitude, ranging from nearly 10^{-3} to 10^{5} cd/m^2. Images obtained by SOS camera equipment will operate on a 10^{2} cd/m^2 scale, causing saturation and pattern distortions. An example of this fact is illustrated on figures 1 and 2. Figure 1 illustrates a considerable amount of saturated pixel values and their regions on RGB and HSL color spaces for a

[1] It is important to notice the difference between HSL color saturation (S), from of pixel value saturation (PVS) The former, is the name of the color space dimension. The latter is a distortion caused by a pattern that spans above the end of color scale.

blue sky pattern. Figure 2 show the saturation points indicated by saturation of blue SB, saturation of green SG and total saturation ST labels. It is important to notice that on the saturated region SAT, is not possible to discriminate between a cloud, a saturated cloud a saturated blue sky pixel, because they have the same end of scale value. The present technologies are slowly overcoming these limitations with high contrast monitors, new file formats and *High Dynamic Range Imaging* (HDRI) (Inanici & Navvab, 2006; Reinhard et al., 2005; Debevec & Malik, 1997; Moeck & Anaokar, 2006). However, they are not presently available at everyday meteorologic and photo-voltaic settings and their usage is left as a suggestion for future research work. Currently, the state-of-the-practice is limited to adapt a logarithmic luminance task environment to a linear camera sensor. As a consequence patterns are distorted or trimmed on high-intensity regions.

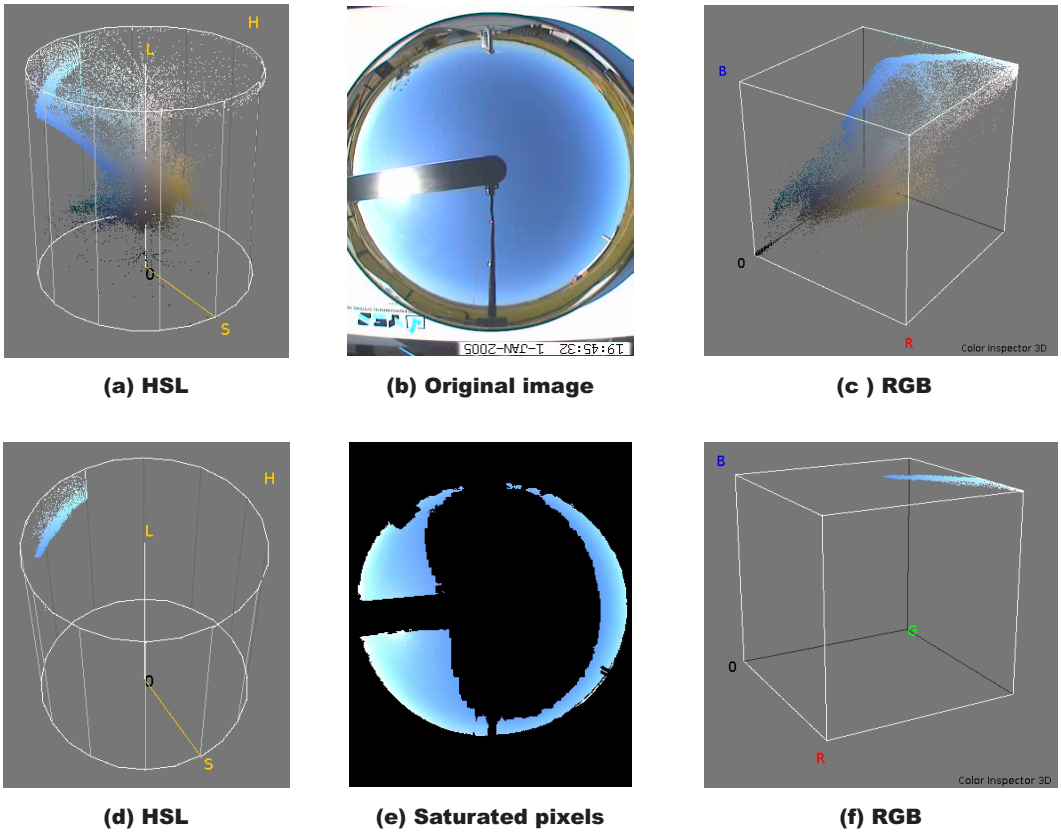

(a) HSL **(b) Original image** **(c) RGB**

(d) HSL **(e) Saturated pixels** **(f) RGB**

Figure 1. All sky images taken on Jan 1^{st} 2005 at 19:45 GMT illustrating saturation problems on image. On first row, the original image and its respective pixel distribution on HSL and RGB color spaces. On the second row only saturated pixels are illustrated on image and their respective pixel distributions on HSL and RGB color spaces. Equipment self image, shading band, camera support, surrounding obstructions and non saturated pixels data were masked to black.

4 Material and methods

In this section we will describe our experimental set up, our dataset and data acquisition parameters and the methodology we followed in order to develop our approach.

4.1 Experimental set up

Our experiment was deployed at the Brazilian Space Research Institute (INPE) Southern Observatory station (SMS) (http://sonda.ccst.inpe.br/basedados/saomartinho.html) located in São Martinho da Serra City, Rio Grande do Sul State, Brazil LAT.: 29° 26′ 34" S ($-29,4428°$), LONG.: 53° 49′ 23" W ($-53,8231°$), ALT.: $489m$. The sky imager site is also co-located with a solar sun photometer (AERONET) , (http://aeronet.gsfc.nasa.gov/) , a BSRN-compatible station (http://www.bsrn.awi.de/), a Brewer Spectrophotometer, UV sensors, etc. A detailed description of the environment and the data can be found in (S. L. Mantelli Neto et al., 2014). The dataset is freely available at (S. Mantelli Neto & von Wangenheim, 2019).

The equipment used to obtain the images was a TSI-440A manufactured by YANKEE Environmental (http://www.yesinc.com). It belongs to the SONDA project (http://sonda.ccst.inpe.br/index.html). TSI acquires an image obtained from a reflector with an observation angle of 160°. The resident software system allows images to be obtained automatically at selected intervals, only when the Sun above 5° of elevation. The resident program was changed in order to obtain images at lower elevation angles too. Image resolution of TSI is $352x288$ or 101376 pixels per image. Nearly 50 % of the image pixels generated by the sky imager was not useful because they record horizon obstructions (poles, buildings, etc.), equipment self-image and a mirror shading band. A total of 1630 images were analyzed, starting January 2005. Images were acquired in JPG file format during daylight every 15 minutes at Greenwich Mean Time (GMT).

We made the whole dataset we acquired for this work publicly available at our site. The dataset includes sky imager data and image masks and is available at (http://www.lapix.ufsc.br/sky-monitoring-surface-cameras). The dataset is composed of two .zip files: *Images* and *Masks*.

4.2 Parametrization of task environment

Atmospheric patterns have their volumetric distributions on color space distorted due to saturation of camera scale. Figure 2 illustrates the distribution of most common sky patterns on two different color spaces HSL and RGB. Arrows are labeled and used to indicate similar regions on image and both color spaces. Figure 2 (a) illustrates a typical blue sky, or *Rayleigh Scattering Pattern* (Lillesand & Kiefer, 1994, sec. 1.3), (Naylor, 2002, sec. 1.2) indicated on the figure as **RAYL**. **RAYL** was parametrized by a Bayesian method using supervised learning guided by exploratory data analysis (EDA) and multivariate statistical analysis (MSA). Three clear sky images sampled from different days, showing different luminance conditions were used as a reference sample (S. L. Mantelli Neto et al., 2014, sec. 2.6.6). Non-sky pixels representing equipment self-image, shading band, poles, building obstructions and surrounding horizon also indicated on figure 2, were considered outliers and manually removed by masking.

We defined the **RAYL** pattern was as a ground truth (GT) by an average, a covariance and an error matrices indicated on equation 1.

$$\mathbf{RAYL} = \begin{vmatrix} 88.65 \\ 128.48 \\ 191.90 \end{vmatrix} + \begin{vmatrix} 147.90 & 190.11 & 235.32 \\ 190.11 & 275.95 & 342.42 \\ 235.32 & 342.42 & 456.11 \end{vmatrix} + \begin{vmatrix} 0.035 \\ 0.049 \\ 0.062 \end{vmatrix} \tag{1}$$

After parameterization of **RAYL** GT patterns, unknown pixels could be classified using the linear Mahalanobis distance (MD) (Mahalanobis, 1936), also known as statistical distance (A. R. Johnson & Wichern, 2007). MD has F-distribution and could be calculated according to the equation 2 recommended by Mahalanobis

$$D^2 = n(\mathbf{x} - \mu)^T \cdot \Sigma^{-1} \cdot (\mathbf{x} - \mu) \tag{2}$$

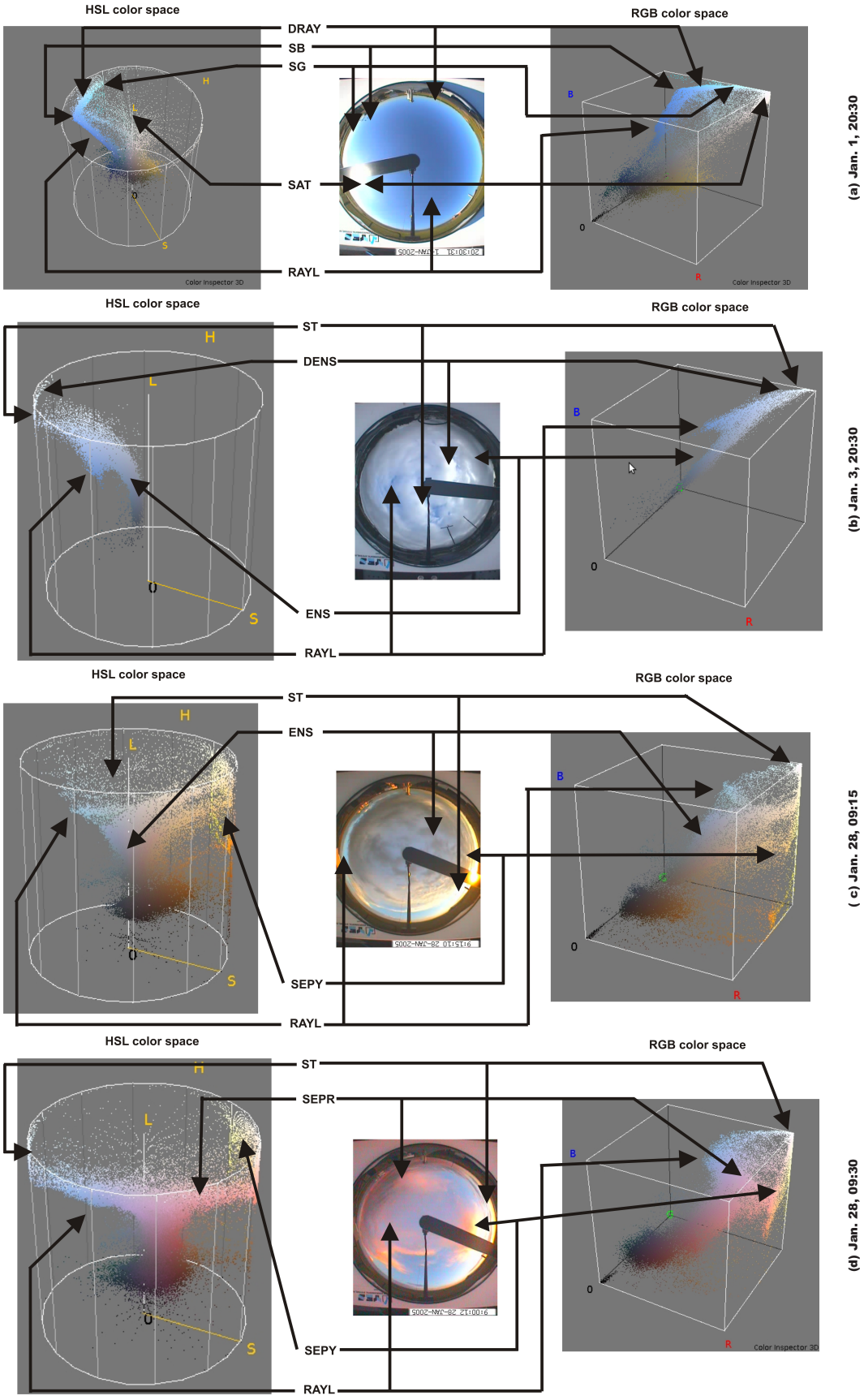

Figure 2. Sample images showing RGB and HSL pattern *loci*. A clear sky on (a), a cloudy sky on (b), a partly cloudy sky yellow colors on (c) and a partly cloudy sky red colors on (d).

where, D^2: is the pixel squared MD from the GT pattern being classified, **x** (r,g,b): is the pixel vector to be classified, represented by its color dimensions, μ: is the average GT vector, T: is the transpose matrix operation, $^{-1}$: is the inversion matrix operation, n: is the number of pixels used to determine the GT, Σ: is the GT covariance matrix. The Mahalanobis distance, when used to generate a customized color-space, is based upon a space generated from the covariance matrix of a set of reference pixel-values that represent typical values for a given phenomenon. It has been employed successfully in the past by the authors in several different environments (Sobieranski et al., 2009) (Sobieranski et al., 2011) (de Carvalho et al., n.d.).

We established a discrimination threshold based on pixel values using F-scores on the same way as the traditional hypothesis testing. Statistical tables are easily found on related literature according to degrees of freedom on the formula suggested by (A. R. Johnson & Wichern, 2007, chap. 5) and illustrated in the equation 3;

$$D^2 \leq \frac{(n-1)p}{(n-p)} F_{p,n-p,(\alpha)} \tag{3}$$

where, p: is the degrees of freedom corresponds to the number of color space dimensions (p = 3), n-p: is the degree of freedom of the GT sampled population. If $(n-p) \geq 120$ the statistics tables consider the degree of freedom to be infinite (∞), $\alpha = 0,05$: is the level of confidence established for the evaluation test, $F_{p,n-p,(\alpha)}$: is the discrimination threshold from GT. This value is obtained from an percentage point from a F-distribution table. $F_{3,\infty,(0,1)} = 3,78$; $F_{3,\infty,(0,05)} = 2,61$; $F_{3,\infty,(0,01)} = 2,08$.

For practical reasons and large population cases, the distance and threshold values needed to be adjusted according to the application otherwise this criteria could discard many pixels. The threshold values were tuned up to $D^2_{RAYL} = 22.68$.

Figure 2 (a) shows a discontinuity point **SB** caused by the saturation of the blue dimension and a second discontinuity point **SG** caused by the saturation of the green dimension on the **RAYL** pattern. In this case the multivariate model is not valid for that region, due to a discontinuity. Mathematically the saturated portion of **RAYL** could be defined as a function in a different interval. This situation is also indicated on figure 2 (a) as *Diffusion of Rayleigh Scattering* pattern or simply **DRAY**. A different criterion is necessary to classify **DRAY** because its occurrence *locus* is along the end of the scale planes. Most classification methods existent in literature have difficulties to classify **DRAY** and ignore or remove it.

A possible physical meaning of this specific saturation is the forward scattering caused by aerosols or water vapor, with a higher optical density near the solar disk or at low solar elevation angles (near the surface horizon) (Long et al., 2009), as illustrated in figures 4(a)-4(d). Although the pattern transitions on camera image from **RAYL** to **DRAY** seems to be *"smooth"* due to pattern whitening; in the color space this transition is *"abrupt"*. We believe that this discontinuity in the color space imposes a certain difficulty on classification methods that erroneously consider a continuous distribution as given in the analysis. Some approaches prefer to discard **DRAY** pixel data from its analysis (Qingyong et al., 2011). **DRAY**, however, still means mostly clear sky and represents a significant amount of image pixels that need to be classified. Pixels in the last region in the figure are near their full saturation value, indicated in the figure as **SAT**. For clarity, the **SAT** point on first column of figure 2 (a) is coincident to the center of HSL top circle. Classification of **DRAY** and **SAT** is made by separating saturated blue dimension of pixel values obtained after determination of the Euclidean Geometric Distance (EGD) *locus* (S. L. Mantelli Neto et al., 2014, sec. 2.6.2), according to described by the equation 4. *EGD* is used because it considers the geometric location of pixels.

$$\mathbf{DRAY} = [(B \geq 255) \ \ \mathbf{AND} \ \ (EGD \geq 52.5)] \tag{4}$$

A typical distribution of patterns could also be noticed on a partially covered sky as illustrated on figure 2 (b). White clouds or *Non-Selective Scattering* pattern **NSS** (Lillesand & Kiefer, 1994, sec. 1.3) also have a typical distribution in the color space. Heavy gray clouds occur continuously in white cloud patterns inside the color space due to cloud thickening, but with smaller values of luminance (S. L. Mantelli et al., 2010). The same multivariate Bayesian method and *criteria* were used to parameterize **NSS** (S. L. Mantelli Neto et al., 2014, sec. 2.6.5). A *GT* pattern was defined as a ground truth (GT) by the average, covariance and an error matrices indicated on equation 5.

$$\mathbf{NSS} = \begin{vmatrix} 141.61 \\ 160.07 \\ 174.01 \end{vmatrix} + \begin{vmatrix} 889.144 & 944.645 & 1039.041 \\ 944.645 & 1092.758 & 1214.737 \\ 1039.041 & 1214.737 & 1390.940 \end{vmatrix} + \begin{vmatrix} 0.076 \\ 0.085 \\ 0.096 \end{vmatrix} \tag{5}$$

The pattern tune-up for classification of **NSS** using the Mahalanobis distance, indicated an statistical threshold value of $D^2_{NSS} = 29.1$.

A discontinuity region was also observed in the distribution of **NSS** and is indicated as **ST** on figure 2 (b). This saturation was observed on several images and is denoted in the present work as *Diffusion of Non-Selective Scattering* pattern **DNSS**. Classification of **DNSS** occurrences is performed by separating the B blue dimension saturated pixel values obtained after determination of the Euclidean Geometric Distance (EGD) *locus* (S. L. Mantelli Neto et al., 2014, sec. 2.6.1), according to described by logic and arithmetic equation 6.

$$\mathbf{DNSS} = (B \geq 255) \ \ \mathbf{AND} \ \ (EGD \leq 52.5) \tag{6}$$

Additionally, extended observation intervals during daylight using the sky imager has shown the presence of new patterns, not previously reported by any reviewed method. Although they were obviously present, as illustrated in figures 2 (c) and 2 (d). By sunset and sunrise, two color patterns in yellow and red could be noticed on sky scenes sometimes simultaneously to white and gray clouds. Those patterns occur when the hues of Sunlight after sunset (or before sunrise) is reflected by clouds (Naylor, 2002, sec. 4.3), (Richards, 1995). Those two patterns occurs at different *locus* in color space, meaning clouds and were defined as distinct ones.

A yellow pattern is noticed when the sun is a bit higher above horizon indicating a *Selective Scattering Pattern in Yellow* (Naylor, 2002, sec. 1.2), in the present research denoted as **SEPY** (S. L. Mantelli Neto et al., 2014, sec. 2.6.3). The figure 2 (c) illustrates *locus* occurrences of **SEPY** patterns in the HSL and RGB linear color spaces.

For the definition of **SEPY** patterns, a typical image was selected possessing a clear evidence of its presence, as illustrated in figure 2 (c). All the other patterns were cleared out by masking them from the image, and only **SEPY** was left (S. L. Mantelli Neto et al., 2014, sec.2.6.3). After the analysis of pattern occurrence, it was noticed that the best way to classify **SEPY** was by pixel hue value H interval discrimination of the HSL color space. Typical values were extracted and refined from image samples and defined by the logic and arithmetic equation 7.

$$\mathbf{SEPY} = \{\forall H \in [0,1] \mid (H > 0.0833) \ \ \mathbf{AND} \ \ (H <= 0.1667)\} \tag{7}$$

Red pattern is noticed when the sun is a bit lower when compared to yellow, indicating a *Selective Scattering Pattern in Red*, in the present research indicated as **SEPR**.

The figure 2 (d) illustrates a *locus* occurrence of **SEPR** pattern in the HSL and RGB linear color spaces. Saturation was also noticed in the **SEPY** and **SEPR** pixel values. However, the discriminating method used based on Hue angle, allowed a precise separation even in the presence of saturated values. Hue angle discrimination was not used to separate **RAYL** and **NSS** patterns, because they occur in coincident hue angles and are very difficult to discriminate.

For the definition of the **SEPR** pattern, a typical image possessing a clear evidence of its presence was also selected. All other patterns were cleared out by masking and only **SEPR** was left (S. L. Mantelli Neto et al., 2014, sec. 2.6.4). After analyzing the image and the pattern occurrence, we noticed that the best way to classify **SEPR** was by hue H pixel value discrimination of the HSL color space. The **SEPR** *locus* is very distinct from the other patterns and can be easily discriminated employing this method. Typical values were extracted and refined from image samples and defined by the logic and arithmetic equation 8.

$$\mathbf{SEPR} = \{\forall H \in [0,1] \mid (H <= 0.0833)\} \tag{8}$$

We chose a hierarchic order to be used in the classification of individual pixels, with a stepwise masking-out of the already classified pixels, in order to analyze saturated regions with higher pixel values prior to non-saturated ones. Otherwise, the algorithm will not properly classify the patterns. Table 2 describes the resume of the principal criteria used for classification in the present work. After the definition of the criteria used for pattern classification, they were implemented using a software prototype to generate the results. Figure 3 illustrates the stepwise hierarchical application of the proposed color-metric.

Table 2. Principal classification criteria proposed in the present research; h is the hierarchical order, the Pattern attributed and the meaning.

h	Criterion of classification	**Pattern**	**Meaning**
1	$\{\forall R,G,B \in [0,255] \mid ((B \geq 255)$ **AND** $(EGD \leq 52,5))\}$	DNSS	cover
2	$\{\forall R,G,B \in [0,255] \mid ((B \geq 255)$ **AND** $(EGD \geq 52,5))\}$	DRAY	clear
3	$\{\forall H \in [0,1] \mid (H > 0.0833)$ **AND** $(H <= 0.1667)\}$	SEPY	cover
4	$\{\forall H \in [0,1] \mid (H <= 0.0833)\}$	SEPR	cover
5	$D^2_{NSS} \leq F_{p,n-p,(\alpha)} = 29,01$	NSS	cover
6	$D^2_{RAY} \leq F_{p,n-p,(\alpha)} = 22,68$	RAY	clear
7	Non classifiable on above cases	NC	undetermined

5 Results

Current method was applied on 1630 surface images. The detailed method developed with parameters, results and comparison with related literature on nearly 7000 images, figures, tables, and charts are too massive to be included in the present document. They are made available as a 511 page technical report (S. L. Mantelli Neto et al., 2014). The representative set of images on figure 4 shows original and analyzed images of mixed, clear, cloudy conditions illustrating the proposed classification patterns. Figure 5 indicates the segmentation color codes used on next figures.

Figures 4(a)-4(d) highlight the significant amount of saturated pixels classified as **DRAY** in light blue. Some methods found on related literature have more difficulty to classify higher intensity pixels specially when the sun is at lower solar elevation angles

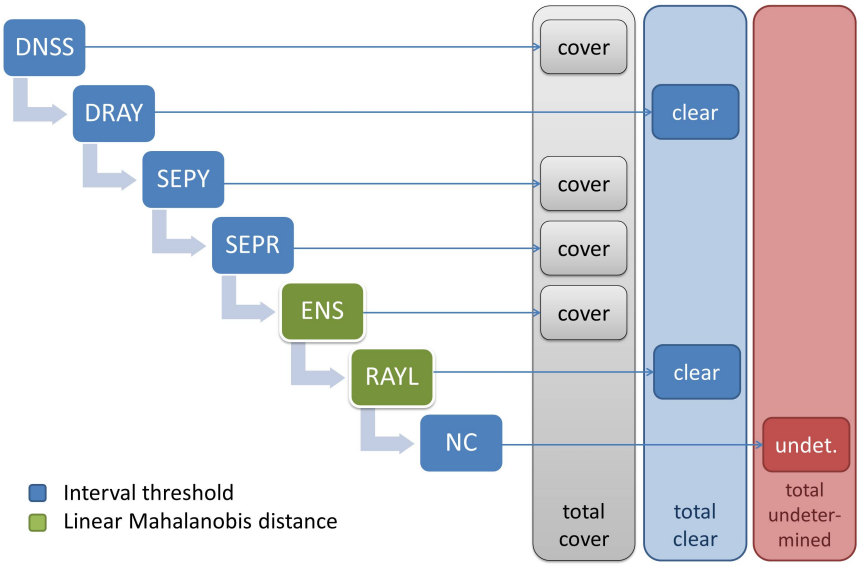

Figure 3. Hierarchical step-wise application of our color similarity metric. The classes *cover*, *clear* and *undetermined* are additive.

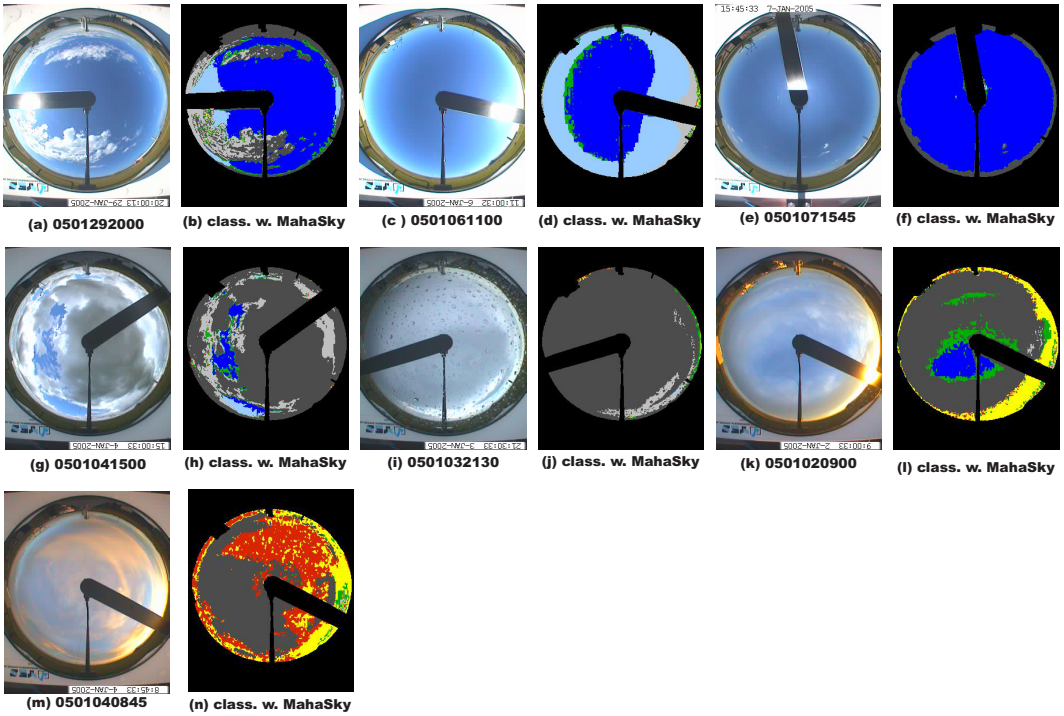

Figure 4. Original images and analysis results for various sky, ranging from clear through covered and presenting lower solar elevation.

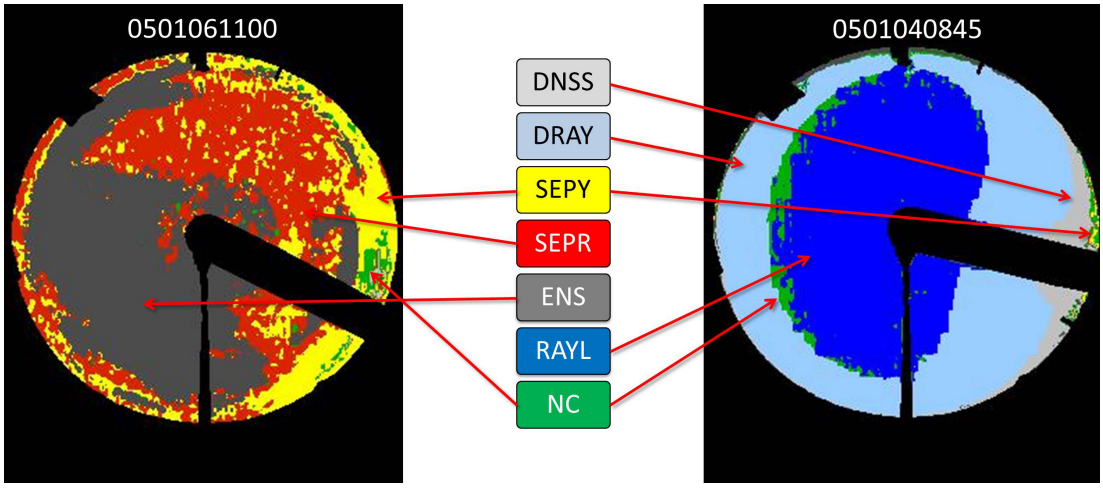

Figure 5. Detail of the results for two different images showing the color-code also employed in figure 4, 7 and 8.

or longer slant optical path. Additional evidence of this fact could be observed when we plot all occurrences of **DRAY** or saturated pixels obtained from all analyzed images as described on figure 6. The occurrence of other patterns like **DNSS**, **SEPY**, **SEPR** also increased with longer slant optical path, although in small proportions. Figures 4(e)-4(f) illustrates a (RAYL) in darker blue on a clear sky at higher solar elevations where in general, the classification methods perform without difficulty. Figures 4(g)-4(j) illustrates a covered sky where could be noticed saturated pixels or **DNSS** pattern in light gray. Figures 4(k)-4(l) illustrates **SEPY** pattern and Figures 4(m)-4(n) illustrates **SEPR** pattern respectively in yellow and red colors. It is important to notice that **SEPY** and **SEPR** are not possible to be determined by 2-D classification approaches, because the green dimension is not considered. Finally, the **NC** pattern in green occurs mostly at the transition between **RAYL** and **NSS** where thresholding could be improved by refining. Few methods deal with **NC** patterns that could reach up to 60% at very low solar elevations with extremely dim light conditions. This NC amount could explain two effects: (i) the reason there is a small bias among different methods and (ii) why some classification methods avoid analyze images at low solar elevations ($< 5°$) under little light conditions. A full month of all sky image analysis where all the above-mentioned situations were classified could be observed in figure 7. This kind of data could be latter on used on the assessments, comparisons and validation of solar energy reaching the surface.

Figure 8 shows the detailed analysis of a mixed cloud condition day with occurrence of all proposed patterns and compares the results with a dicotomizer method.

5.1 Validation

Some aspects have to be considered concerning the methods to be compared for this validation, since they have to be subject to the *same sources of variability* (Montgomery, 2005, ch. 1). Although the present method was implemented in the 3-dimensional domain, it is being compared with a 2-dimensional domain method. We employed a look-up table method, using the *clear/cover* classification obtained from table 2 to convert the results to binary all-sky dichotomizer approach for the sake of our comparison. It is important to notice that there is no correspondence of NC pattern on dichotomizer. This will cause small aleatory difference on results.

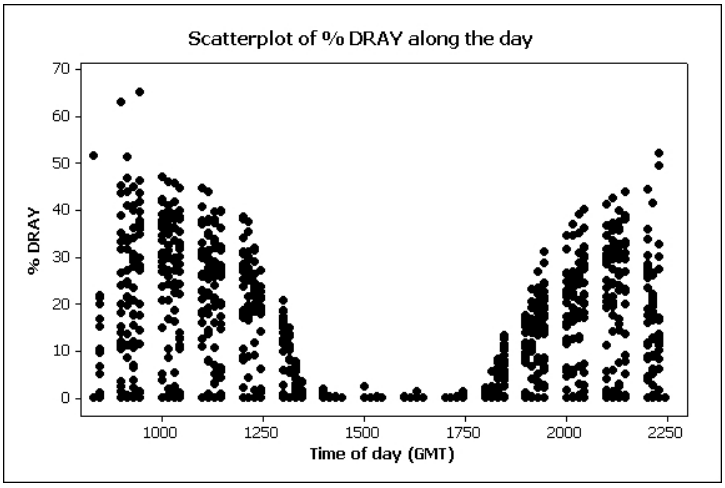

Figure 6. Percentage of **DRAY** daily occurrences for January 2005.

After conversion, the proposed method (MahaSky) was statistically paired compared to Long (Long et al., 2006) and EGD (S. L. Mantelli Neto et al., 2014) methods, and their differences are illustrated on figure 9.

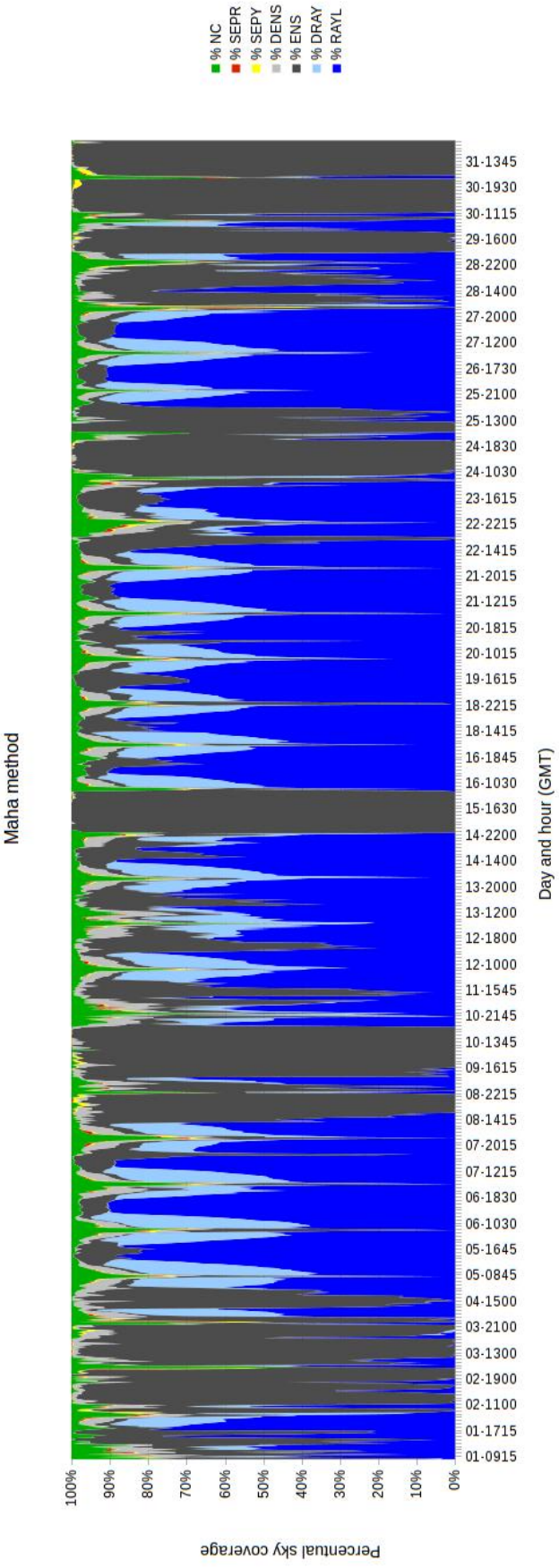

Figure 7. Cloud coverage estimation using the Maha method for January 2005.

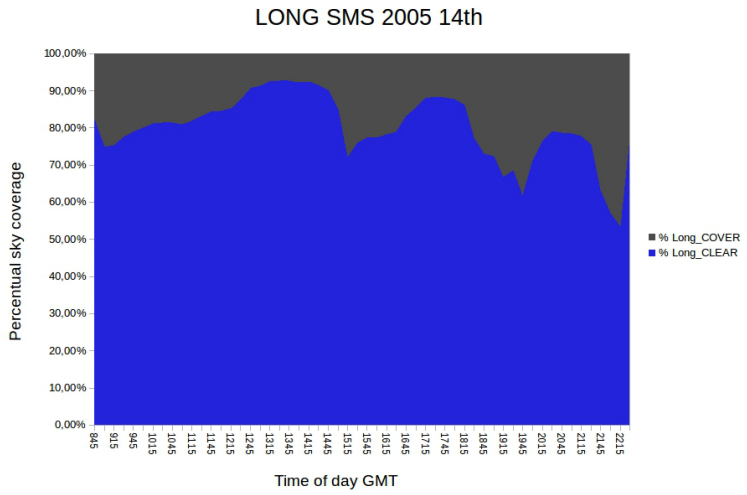

(a) Long Method

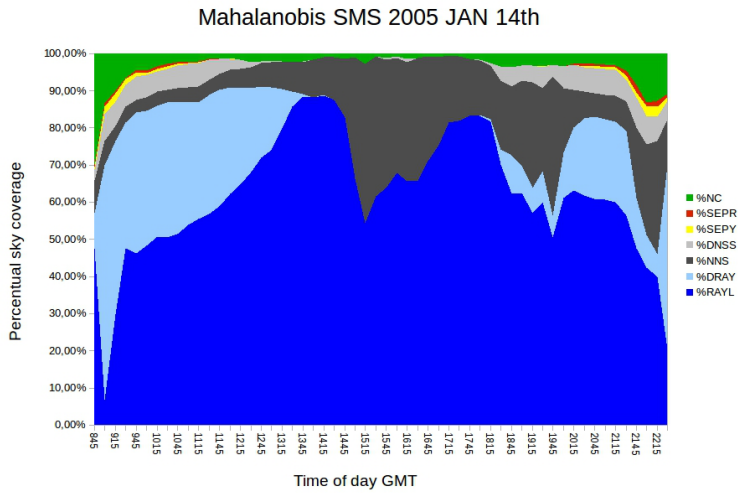

(b) Maha method

Figure 8. One day data comparison between a dichotomizer and Maha methods for January 14th 2005.

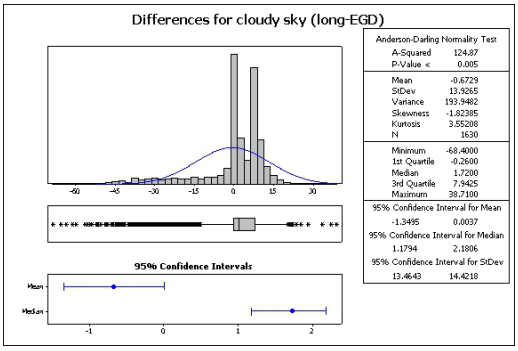

(a) Long and EGD Methods

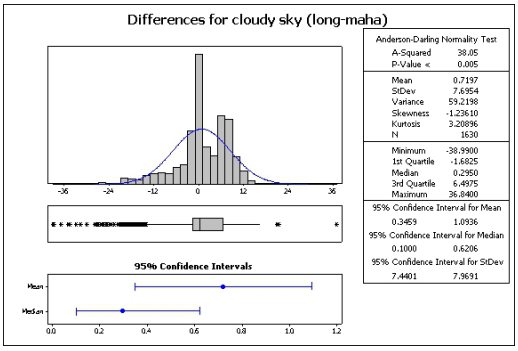

(b) Long and Maha Methods

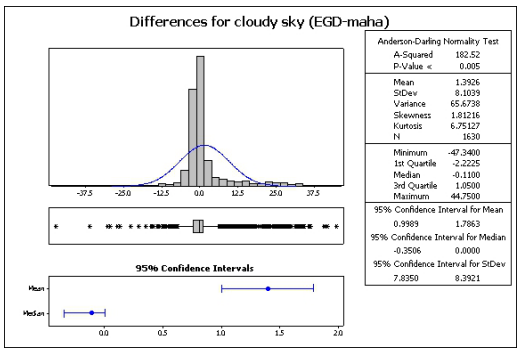

(c) EGD and Maha Methods

Figure 9. Paired comparison of differences in cloud coverage estimation among methods for January 2005.

The paired differences on 1630 images among the proposed downgraded method and two other ones existent on literature, were checked by hypothesis testing. Analysis indicated that z-scores differences existent were bellow the critical values, indicating that methods are similar, and aleatory factors caused the differences. Differences could also be due to the establishment of a different task domain dimension used during analysis. Another difference noticed was the different training data set used to define the parameters, which are subject to distinct meteorological and atmospheric conditions. The **NC** pattern not used on (Long et al., 2006) method could introduce a bias because it does not consider the NC class on pixel for analysis.

6 Conclusions

Current methods presented in the literature, allied to camera restrictions, limit the overall performance and, consequently, the quality of the results in monitoring the sky for cloud coverage estimation. This indicates that the more features are available for cloud classification, the better will be the conditions to classify cloud types, species, and varieties.

Additionally, we presented a new methodology for classification of sky patterns using surface cameras. A key feature of the method is that it does not focus only on the development of a new pixel classification algorithm but considers several aspects of Synoptic Observation Systems (SOS) as a whole. Common practices used by related works during classification, like dichotomizers and reduction of dimensionality were not employed in this work. Dichotomizer methods were not used for two reasons. Dichotomizer does not handle properly false positives and negatives because they are assigned to either one or other pattern. The dichotomizer does not handle multi-category patterns, necessary for the implementation of the proposed method. Reduction of dimensionality causes loss of information to be classified.

3-dimensional analysis on RGB and HSL color spaces allowed the proposed method to obtain more information from sky data. One example is the better usage of the luminance diagonal on the whole RGB color space, which spans the interval [0,442], against [0,361] for 2-D and [0,255] for 1-D counterparts . Exploratory Data analysis indicated that patterns, existent on logarithmic luminance scale domain are distorted due to signal saturation by linear systems used to monitor and store data. Until the present technology does not develop systems that match the human perceived luminance scale, additional patterns were presented in a more appropriate approach, according to atmospheric physics by considering them discontinued functions intervals as follows. Rayleigh scattering in blue (RAYL), non-specific scattering indicated by clouds (NSS), selective scattering in red (SEPR) and yellow (SEPY) colors, saturation of Rayleigh scattering caused by forward scattering (DRAYL) and saturation of non-specific scattering indicated by clouds (DNSS). New proposed patterns allowed an appropriate analysis of the images bellow 5° of solar elevation, allowing the extension of the daylight observation period. The image dataset employed in this work is freely available at (S. Mantelli Neto & von Wangenheim, 2019).

6.1 Limitations and Future Work

It is possible that the model may require some adjustment to take into account seasonal or local variability. A better classification could be achieved if the full pattern distribution was not trimmed by saturation and distortions were not limited by linear sensor response. A combination of techniques to detect different features could also be used to produce a more meaningful result.

Another limitation of this approach is that it, as do all the other models we investigated, does not take into consideration spatial context information of the pixels in the

image. It is a method that operates exclusively in the domain of pixel values, classifying each pixel independently and without taking into consideration any information that could be gained from its surroundings. Observing figures 4 and 5 it is possible to observe that NC patterns sometimes appear in boundaries between regions, as in fig.4(d) and (h), where NC forms boundaries between $DRAY$ and $RAYL$ and between NSS and $RAYL$ regions respectively, and sometimes NC patterns appear exclusively inside other patterns, as in fig.4(l), where the NC pattern is contained inside a $SEPY$ region. One could postulate that, when NC patterns occur inside homogeneous regions or in boundaries between regions that have the same *meaning*, as in $DRAY$ and $RAYL$ in fig.4(d), they can be computed to the total area of that specific *meaning*. These issues are left as suggestions for future investigation and implementation.

7 Acknowledgements

The authors would like to thank INPE operational teams of INPE/CPTEC/LIM (http://lim1.cptec.inpe.br/lim/in), and INPE/CRS/OES (http://www.inpe.br/crs/institucional.php) and INPE/CCST/LABREN (http://www.ccst.inpe.br/) and the research team of UFSC-INCOD (http://www.incod.ufsc.br/?lang=en), specially to Luís Gustavo Lorgus Decker for helping with image masking. We also like to thank the grants from FINEP by SONDA project (22.01.0569.00), PETROBRAS (0050.0029348.07.4) and CNPQ by HIDROCAM project (478694/2011-3).

References

Bojanowski, J. S., Donatelli, M., Skidmore, A. K., & A., V. (2013, November). An auto-calibration procedure for empirical solar radiation models. *Environmental Modelling & Software*, *49*, 118-128. Retrieved from `http://www.sciencedirect.com/science/article/pii/S1364815213001801` doi: 10.1016/j.envsoft.2013.08.002

Bradley, E., Roberts, D., & Still, C. (2010, January 2010). Design of an image analysis website for phenological and meteorological monitoring. *Environmental Modelling & Software*, *25*(1), 107-116. doi: 10.1016/j.envsoft.2009.07.006

Cazorla, A., Husillos, C., Antón, M., & Alados-Arboledas, L. (2015). Multi-exposure adaptive threshold technique for cloud detection with sky imagers. *solar energy*, *114*, 268-277. Retrieved from `http://ac.els-cdn.com/S0038092X1500064X/1-s2.0-S0038092X1500064X-main.pdf?_tid=de4a79a6-704a-11e6-88aa-00000aacb362&acdnat=1472737934_8a2de6b8f6a1d0dd864291ab50d6598c` doi: http://dx.doi.org/10.1016/j.solener.2015.02.006

Cazorla, A., Olmo, F. J., & Alados-Arboledas, L. (2008). Development of a sky imager for cloud cover assessment. *Journal of the Optical Society of America*, *25*(1), 29–39. doi: http://dx.doi.org/10.1364/JOSAA.25.000029

Cess, R. D., Zhang, M. H., Minnis, P., Corsetti, L., Dutton, E., Forgan, B., ... Zhou, Y. (1995). Absorption of solar radiation by clouds: Observations versus models. *Science*, *267*(5197), 496-499. doi: 10.1126/science.267.5197.496

Debevec, P. E., & Malik, J. (1997). *Recovering high dynamic range radiance maps from photographs* (Tech. Rep.). University of California at Berkeley. Retrieved from `http://www.cs.berkeley.edu/~malik/papers/debevec-malik97.pdf`

de Carvalho, L. E., Neto, S. M., Sobieranski, A., Comunello, E., & von Wangenheim, A. (n.d.). Improving graph-based image segmentation using nonlinear color similarity metrics. *International Journal of Image and Graphics*, *15*(4), 1550018.

Duda, R. O., Hart, P. E., & Stork, D. G. (2001). *Patterns classification* (2nd ed.). John Wiley & Sons. Retrieved from `http://www.wiley.com/WileyCDA/`

WileyTitle/productCd-111858600X.html

Feister, U., & Shields, J. (2005, 10). Cloud and radiance measurements with the vis/nir daylight whole sky imager at lindenberg (germany). *Meteorologische Zeitschrift*, *14*(5), 627-639. Retrieved from http://dx.doi.org/10.1127/0941-2948/2005/0066 doi: 10.1127/0941-2948/2005/0066

Feister, U., Shields, J., Karr, M., Johnson, R., Dehne, K., Woldt, M., ... Potsdam, M. O. (2000). *Ground-based cloud images and sky radiances in the visible and near infrared region from whole sky imager measurements.* Retrieved from http://jshields.ucsd.edu/publications/pdfs/22%20Feister%202000.pdf

Gonzalez, R. C., & Woods, R. E. (2002). *Digital image processing* (2nd ed.). Prentice Hall.

Gonzalez, R. C., & Woods, R. E. (2007). *Digital image processing* (3rd ed.). Prentice Hall. Retrieved from http://folk.uio.no/ainard/Folder2/Digital%20Image%20Processing%203rd%20ed.%20-%20R.%20Gonzalez,%20R.%20Woods.pdf

Grossberg, M. D., & Nayar, S. K. (2003). Determining the camera response from images: What is knowable? *IEEE TRANSACTIONS ON PATTERN ANALYSIS AND MACHINE INTELLIGE*, *25*(11), 1455-1467. Retrieved from http://ieeexplore.ieee.org/stamp/stamp.jsp?arnumber=1240119 doi: 10.1109/TPAMI.2003.1240119

Harrison, R. G., Chalmers, N., & Hogan, R. J. (2008). Retrospective cloud determinations from surface solar radiation measurements. *Atmospheric Research*, *90*, 54-62. doi: 10.1016/j.atmosres.2008.04.001

Hu, Y., & Stamnes, K. (2000). Climate sensitivity to cloud optical properties. *Tellus*, *52*, 81 - 93. doi: 10.1034/j.1600-0889.2000.00993.x

Inanici, M. N., & Navvab, M. (2006). The virtual lighting laboratory: Per-pixel luminance data analysis. *LEUKOS*, *3,2*, 89?104. doi: 10.1582/LEUKOS.2006.03.02.001

Iqbal, M. (1983). *An introduction to solar radiation.* New York Academic Press.

Jain, A., Duin, R., & Mao, J. (2000, Jan). Statistical pattern recognition: a review. *Pattern Analysis and Machine Intelligence, IEEE Transactions on*, *22*(1), 4-37. doi: 10.1109/34.824819

Johannet, A., Vayssade, B., & Bertin, D. (2007). Neural networks: From black box towards transparent box application to evapotranspiration modeling. *World Academy of Science, Engineering and Technology*, *30*, 162-169. Retrieved from http://www.waset.org/journals/waset/v30.php

Johnson, A. R., & Wichern, D. W. (2007). *Applied multivariate statistical analysis* (6th ed.). Pearson Education International. Retrieved from https://www.pearsonhighered.com/program/Johnson-Applied-Multivariate-Statistical-Analysis-6th-Edition/PGM274834.html

Johnson, H. W. S. J., R. (1989.). *Automated visibility and cloud cover measurements with a solid-state imaging system.* (Tech. Rep. Nos. 89-7, GL-TR-89-0061). University of California, San Diego, Scripps Institution of Oceanography, Marine Physical Laboratory, SIO Ref. Retrieved from file:///home/sylvio/Downloads/ADA216906.pdf (128 pp.)

Kasten, F., & Czeplak, G. (1980). Solar and terrestrial radiation dependent on the amount and type of cloud. *Solar Energy*, *24*(2), 177 - 189. Retrieved from http://www.sciencedirect.com/science/article/pii/0038092X80903916 doi: https://doi.org/10.1016/0038-092X(80)90391-6

Kazantzidis, A., Tzoumanikas, P., Bais, A., Fotopoulos, S., & Economou, G. (2012). Cloud detection and classification with the use of whole-sky ground-based images. *Atmospheric Research*, *113*(0), 80 - 88. Retrieved from http://www.sciencedirect.com/science/article/pii/S0169809512001342 doi: http://dx.doi.org/10.1016/j.atmosres.2012.05.005

Koslof, T. (2006). *Visualizing high dynamic range images* (Tech. Rep.). University of California at Berkley. Retrieved from http://vis.berkeley.edu/courses/cs294-10-sp06/wiki/images/5/52/ToddWriteup.pdf

Kreuter, A., Zangerl, M., Schwarzmann, M., & Blumthaler, M. (2009). All-sky imaging: a simple, versatile system for atmospheric research. *Applied Optics*, *48*, 1091 - 1097. Retrieved from http://www.opticsinfobase.org/DirectPDFAccess/503B44E9-BDB9-137E-C455BA62A9D969C4_176587.pdf?da=1&id=176587&seq=0 doi: 10.1364/AO.48.001091

Kurtz, B., Mejia, F., & Kleissl, J. (2017, December). A virtual sky imager testbed for solar energy forecasting. *Solar Energy*, *158*, 753-759. Retrieved from https://www.sciencedirect.com/science/article/pii/S0038092X1730899X doi: https://doi.org/10.1016/j.solener.2017.10.036

Lillesand, T. M., & Kiefer, R. W. (1994). *Remote sensing and image interpretation.* John Wiley & Sons.

Long, C. N., Dutton, E. G., Augustine, J. A., Wiscombe, W., Wild, M., McFarlane, S. A., & Flynn, C. J. (2009). Significant decadal brightening of downwelling shortwave in the continental united states. *Journal of Geophysical Research: Atmospheres*, *114*(D10), n/a–n/a. Retrieved from http://dx.doi.org/10.1029/2008JD011263 doi: 10.1029/2008JD011263

Long, C. N., Sabburg, J. M., Calbo, J., & Page, J. D. (2006, may). Retrieving cloud characteristics from ground-based daytime color all-sky images. *Journal of Atmospheric and Oceanic Technology*, *23*, 633-652. doi: http://dx.doi.org/10.1175/JTECH1875.1

Mahalanobis, P. C. (1936). On the generalized distance in statistics. *Proceedings National Institute of Science. India.* Retrieved from http://ir.isical.ac.in/dspace/handle/1/1268

Mantelli, S. (2001). *Desenvolvimento de uma nova metodologia para a estimativa da cobertura de nuvens usando uma câmera de superfície e comparando com imagens de satélite.* (Master's thesis, Universidade Federal de Santa Catarina, Departamento de Informática e Estatística). Retrieved from http://repositorio.ufsc.br/xmlui/handle/123456789/83106

Mantelli, S. L., v. Wangenhein, A., & Pereira, E. B. (2005). Modelo preliminar de estimativa de cobertura de nuvens, no espaco de cores rgb obtidas a partir de imageador automático. In *Proc. xii symp. brasileiro de sensoriamento remoto, goiania brazil.* (p. 4123-4131). Retrieved from http://urlib.net/ltid.inpe.br/sbsr/2004/11.16.17.23

Mantelli, S. L., v. Wangenhein, A., Pereira, E. B., & Comunello, E. (2010). The use of euclidean geometric distance on rgb color space for classification of sky and cloud patterns. *Journal of Atmospheric and Oceanic Technology*, *27*(9), 1504 - 1517. doi: 10.1175/2010JTECHA1353.1

Mantelli Neto, S., & von Wangenheim, A. (2019). *Sky monitoring surface camera dataset from são martinho da serra, rs, southern brazil.* http://www.lapix.ufsc.br/sky-monitoring-surface-cameras. LAPIX/UFSC.

Mantelli Neto, S. L. (2010). *Desenvolvimento de metodologia para a estimativa da cobertura de nuvens usando uma de câmera de superfície e comparando com as imagens de satélite* (Doctoral dissertation, Universidade Federal de Santa Catarina). Retrieved from http://repositorio.ufsc.br/xmlui/handle/123456789/83106

Mantelli Neto, S. L., Pereira, E. B., Thomaz Junior, J. C., Wangenheim, A. v., Decker, L. G. L., & Coser, L. (2014). *Atmospheric pattern studies from a surface imager during january 2005 at inpe southern regional center, são martinho da serra rs brazil* (Tech. Rep.). INPE (Instituto Nacional de Pesquisas Espaciais INCOD (Instituto Nacional de Convergência Digital). Retrieved from http://urlib.net/sid.inpe.br/mtc-m21b/2014/08.19.17.27

Marquez, R., & Coimbra, C. F. M. (2013). Intra-hour dni forecasting based on

cloud tracking image analysis. *Solar Energy*, *91*, 327-336. doi: http://www.sciencedirect.com/science/article/pii/S0038092X1200343X

Martins, F., Pereira, E., & Abreu, S. (2007). Satellite-derived solar resource maps for brazil under {SWERA} project. *Solar Energy*, *81*(4), 517 - 528. Retrieved from http://www.sciencedirect.com/science/article/pii/S0038092X0600199X doi: http://dx.doi.org/10.1016/j.solener.2006.07.009

Martins, F., Souza, M., & Pereira, E. (2003). Comparative study of satellite and ground techniques for cloud cover determination. *Adv. Space Res.*, *32*(11), 2275-2280. doi: DOI:10.1016/S0273-1177(03)90554-0

Marty, C., & Philipona, R. (2000). The clear-sky index to separate clear-sky from cloudy-sky situations in climate research. *Geophysical Research Letters*, *27*, 2649 - 2652. Retrieved from ftp://ftp.pmodwrc.ch/pub/publications/grl\%20csi.pdf

Mejia, F. A., Kurtz, B., Murray, K., Hinkelman, L. M., Sengupta, M., Xie, Y., & Kleissl, J. (2016). Coupling sky images with radiative transfer models: a new method to estimate cloud optical depth. *Atmospheric Measurement Techniques*, *9*(8), 4151–4165. Retrieved from https://www.atmos-meas-tech.net/9/4151/2016/ doi: 10.5194/amt-9-4151-2016

Mitsunaga, T., & Nayar, S. K. (1999, June). Radiometric self calibration. *Proc. CS Conf. Computer Vision and Pattern Recognition*, *1*, 374-380. Retrieved from http://ieeexplore.ieee.org/xpls/abs_all.jsp?arnumber=786966&tag=1 doi: 10.1109/CVPR.1999.786966

Moeck, M., & Anaokar, S. (2006). Illuminance analysis from high dynamic range images. *Leukos*, *2*(3), 211-228. doi: DOI:10.1582/LEUKOS.2006.02.03.005

Montgomery, D. C. (2005). *Design and analisys of experiments.* John Wiley and Sons Inc.

Nardino, M., & Georgiadis, T. (2003). Cloud type and cloud cover effects on the surface radiative balance at several polar stations. *Theoretical and Applied Climatology*, *74*, 203 - 215. Retrieved from http://www.dvgu.ru/meteo/library/30740203.pdf doi: 10.1007/s00704-002-0708-2

Naylor, J. (2002). *Out of the blue.* Cambridge University Press. Retrieved from http://dx.doi.org/10.1017/CBO9780511536595

Newell, A., & Simon, H. A. (1971). Human problem solving: The state of the theory in 1970. *American Psychologist*, *26*(2), 145-159. Retrieved from http://psycnet.apa.org/journals/amp/26/2/145/ doi: 10.1037/h0030806

Perez, R., Seals, R., & J., M. (1993). All-weather model for sky luminance distribution - preliminary configuration and validation. *Solar Energy*, *50*(3), 235-245. Retrieved from http://www.sciencedirect.com/science/article/pii/0038092X9390017I

Piccardi, M. (2004, October 07). Background subtraction techniques: a review. In *Systems, man and cybernetics, 2004 ieee international conference on* (Vol. 4, pp. 3099–3104 vol.4). IEEE. Retrieved from http://dx.doi.org/10.1109/icsmc.2004.1400815 doi: 10.1109/icsmc.2004.1400815

Qingyong, J., Lu, W., & Yang, J. (2011). A hybrid thresholding algorithm for cloud detection on ground-based color images. *J. Atmos. Oceanic Technol.*, *28*, 1286?1296. doi: http://dx.doi.org/10.1175/JTECH-D-11-00009.1

Qiu, F., & Jensen, J. R. (2004). Opening the black box of neural networks for remote sensing image classification. *International Journal of Remote Sensing*, *25(9)*, 1749-1768. Retrieved from http://www.tandfonline.com/doi/abs/10.1080/01431160310001618798?journalCode=tres20 doi: 10.1080/01431160310001618798

Reinhard, E., Ward, G., Pattanaik, S., & Debevec, P. (2005). *High dynamic range imaging: Acquisition, display, and image-based lighting (the morgan kaufmann series in computer graphics)* (1st ed.). San Francisco, CA, USA: Morgan Kaufmann Publishers Inc.

Richards, J. A. (1995). *Remote sensing digital image analysis* (2nd ed.). Springer-Verlag.

Sabburg, J., & Wong, J. (1999). Evaluation of ground-based sky camera system for use in surface irradiance measurements. *Journal of Atmospheric and Oceanic Technology*, *16*, 752-759. doi: http://dx.doi.org/10.1175/1520-0426(1999)016⟨0752:EOAGBS⟩2.0.CO;2

Schade, N. H., Macke, A., Sandmann, H., & Stick, C. (2008). Total and partial cloud amount detection during summer 2005 at westerland (sylt, germany). *Atmospheric Chemistry and Physics*, *8*, 13479-13505. Retrieved from http://www.atmos-chem-phys.org/9/1143/2009/acp-9-1143-2009.pdf doi: 10.5194/acpd-8-13479-2008

Setiono, R., Leow, W. K., & Thong, J. Y. L. (2000). Opening the neural network black box: an algorithm for extracting rules from function approximating artificial neural networks. In *Proceedings of the twenty first international conference on information systems* (pp. 176–186). Atlanta, GA, USA: Association for Information Systems. Retrieved from http://portal.acm.org/citation.cfm?id=359640.359738

Sobieranski, A. C., Abdala, D. D., Comunello, E., & von Wangenheim, A. (2009). Learning a color distance metric for region-based image segmentation. *Pattern Recognition Letters*, *30*(16), 1496 - 1506. Retrieved from http://www.sciencedirect.com/science/article/pii/S0167865509002098 doi: https://doi.org/10.1016/j.patrec.2009.08.002

Sobieranski, A. C., Comunello, E., & von Wangenheim, A. (2011). Learning a nonlinear distance metric for supervised region-merging image segmentation. *Computer Vision and Image Understanding*, *115*(2), 127 - 139. Retrieved from http://www.sciencedirect.com/science/article/pii/S1077314210002006 doi: https://doi.org/10.1016/j.cviu.2010.09.006

Souza-Echer, M. P., Pereira, E. B., Bins, L., & Andrade, M. A. R. (2006). A simple method for the assessment of the cloud cover state in high-latitude regions by a ground-based digital camera. *Journal of Atmospheric and Oceanic Technology*, *23*(3), 437-447. doi: http://dx.doi.org/10.1175/JTECH1833.1

Tapakis, R., & Charalambides, A. (2013). Equipment and methodologies for cloud detection and classification: A review. *Solar Energy*, *95*, 392 - 430. Retrieved from http://www.sciencedirect.com/science/article/pii/S0038092X12004069 doi: http://dx.doi.org/10.1016/j.solener.2012.11.015

Tsin, Y., Ramesh, V., & Kanade, T. (2001). Statistical calibration of the ccd imaging process. In *Proc. int.conf. computer vision* (Vol. 1, p. 480-487). Retrieved from http://ieeexplore.ieee.org/document/937555/?part=1 doi: 10.1109/ICCV.2001.937555

WMO. (2008). Guide to meteorological instruments and methods of observations. (7th ed.) [Computer software manual]. World Meteorological Organization, 7bis, avenue de la Paix, Case postale 2300, CH-1211 Geneva 2, Switzerland. Retrieved from http://www.wmo.int/pages/prog/gcos/documents/gruanmanuals/CIMO/CIMO_Guide-7th_Edition-2008.pdf (WMO-No. 8 I.15-1 - I.15-11)

Yamanouchi, T., & Charlock, T. P. (1993). Radiative effects of clouds icesheet and sea ice in the antartic. *Proceedings of Yokohama Symposia J2 and J5*, *223*. Retrieved from http://www.cig.ensmp.fr/~iahs/redbooks/a223/iahs_223_0029.pdf doi: 10.1029/96JD02866

Yang, J., Min, Q., Lu, W., Ma, Y., Yao, W., Lu, T., ... Liu, G. (2016). A total sky cloud detection method using real clear sky background. *Atmospheric Measurement Techniques*, *9*, 587 - 597. Retrieved from http://www.atmos-meas-tech.net/9/587/2016/amt-9-587-2016.pdf doi: 10.5194/amt-9-587-2016

Yang, J., Min, Q., Lu, W., Yao, W., Ma, Y., Du, J., ... Liu, G. (2015). An au-

780 tomated cloud detection method based on the green channel of total-sky
781 visible images. *Atmospheric Measurement Techniques*, *8*(11), 4671–4679.
782 Retrieved from `http://www.atmos-meas-tech.net/8/4671/2015/` doi:
783 10.5194/amt-8-4671-2015
784 Zhang, P. G. (2007, January). Avoiding pitfalls in neural network research.
785 *IEEE TRANSACTIONS ON SYSTEMS, MAN, AND CYBERNETICS*
786 *PART C APPLICATIONS AND REVIEWS.*, *37*, 3-16. doi: 10.1109/
787 TSMCC.2006.876059